Granular flow during hopper discharge

J. E. Hilton and P. W. Cleary

CSIRO Mathematics, Informatics and Statistics, Clayton South, VIC 3169, Australia

Granular material freely discharging from a hopper under gravity is one of the oldest and most widely studied problems in granular flow. Despite the apparent simplicity of the system, expressions relating the discharge rate of the hopper to the properties of the individual grains are difficult to determine and typically empirical in nature. A mathematical model for discharge from a hopper is derived based on the dynamics of individual particles just within the outlet. In contrast to previous models, this analysis derives a flow rate from granular dynamics, rather than dimensional arguments. The model, therefore, uses no assumptions about the form of the stress distribution within the hopper, or the addition of empirical factors or fitting parameters. Our model gives a flow rate identical in form to a well-known empirical expression, showing that an experimentally determined constant used in this expression is purely geometry-dependent. Our analysis is also extended to derive an expression for the flow rate incorporating gas drag, which becomes dominant at small grain sizes, significantly reducing the outflow rate. The resulting expression shows excellent agreement with a range of computational simulations using a coupled discrete element and Navier-Stokes method. These simulations also show that the gas flow is much more complex than previously assumed in this region, and simplified assumptions used in prior hopper flow models do not hold.

PACS number(s): 45.70.−n, 47.55.Kf

I. INTRODUCTION

The study of granular flow in hoppers has an extensive history, and the analytical description of granular behavior within a hopper remains an active research area. During discharge, the particulate material exhibits the full range of granular behavior, from static packing within the bed, through yielding from dense to dilute phase flow over the outlet, to a free-falling particle stream. Hopper flow is also of significant importance from a practical aspect. Large-scale hoppers are used for storage and transportation in chemical processing, food manufacture, pharmaceuticals, and agriculture. The flow characteristics of fine powders, in which interstitial gas effects dominate, are also of importance in process design for each of these industries.

In contrast to a liquid-filled column, the pressure at the base of a hopper is constant if $H > D$, where H is the fill height and D is the diameter. This pressure saturation occurs because the weight of the bed is supported by the walls of the hopper, and results in a constant discharge flow rate, Q, if $H > D$ and $D > \frac{5}{2}D_0$, where D_0 is the outlet diameter [1,2]. This effect was first reported by Janssen in 1895 from experiments in corn-filled silos, although it is likely this was known even earlier [3]. On dimensional grounds, the flow rate is of the form $Q = C\rho_b\sqrt{D_0{}^5g}$, where C is a constant depending on the system. This relation was investigated by Beverloo [4] for monodisperse particle distributions in cylindrical hoppers, who found a dependency of this form existed with $C \approx 0.55$–0.65 [5]. It was also determined, however, that the zero outflow rate occurred for a nonzero outlet diameter. Beverloo suggested that "this might be explained by assuming that along the margin of the orifice a zone is useless or less fit for use for the flow" and that the reduced diameter $D_B = D_0 - k\,d$ should be used instead, where d is the particle diameter and $k \simeq 1.5$ is a constant. This gives an expression for the flow rate as

$$Q = C\rho_b\sqrt{D_B^5g}, \tag{1}$$

where ρ_b is a bulk density and g is gravitational acceleration. This relation has been shown to hold for a wide range of grain types in flat-based hoppers [5]. For hoppers with $D_0 \leqslant 6d$, where d is the grain diameter, the flow is intermittent and jamming can occur, so Eq. (1) only holds provided $D_0 > 6d$.

The bulk density in Eq. (1) is given by $\rho_b = \epsilon_b\rho_p$, where ϵ_b is a bed voidage fraction and ρ_p is the particle solid density. The voidage is highly variable over the outlet region, so the choice of voidage fraction in these expressions has been a topic of debate. Beverloo originally used the density of the packing over the hopper, before the hopper had discharged, to define ϵ_b. Huntingdon and Rooney defined a "flowing density" as the ratio of the measured mass flow rate and the volume flow rate, determined by observing the upper surface of the particle bed [5]. Kotchanova suggested using the voidage just above the outlet, as the flow dynamics only involves the particles within this region [6].

A wide range of hopper types, outflow geometries, and particle distributions have previously been studied. For simplicity, we restrict our analysis to cylindrical, flat-based hoppers with a central outlet and a monodisperse, noncohesive, spherical particle distribution. A schematic diagram of this ideal configuration is shown in Fig. 1. The system is also considered closed, so gas flow can only occur through the outlet. The radial symmetry and flat base removes any geometry-dependent effects from the stress field within the hopper, and the choice of spherical monodisperse particles removes any effect of particle size distribution on the outflow rate [7]. Particles discharge through a funnel-shaped region formed by a slowly moving, almost stagnant, zone of particles surrounding the outlet. The funnel is approximately conical with angle β from the vertical. The particle dynamics governing the flow rate occurs in the immediate vicinity of the outlet, where the granular flow transforms from slow dense flow, with long-lasting frictional contacts, to dilute flow. The boundary between these flow types is known as the "free fall arch," which is assumed to be a section of a spherical surface of radius $R_B/\sin\beta$, where $R_B = \frac{1}{2}D_B$, spanning the hopper outlet. This is shown schematically in
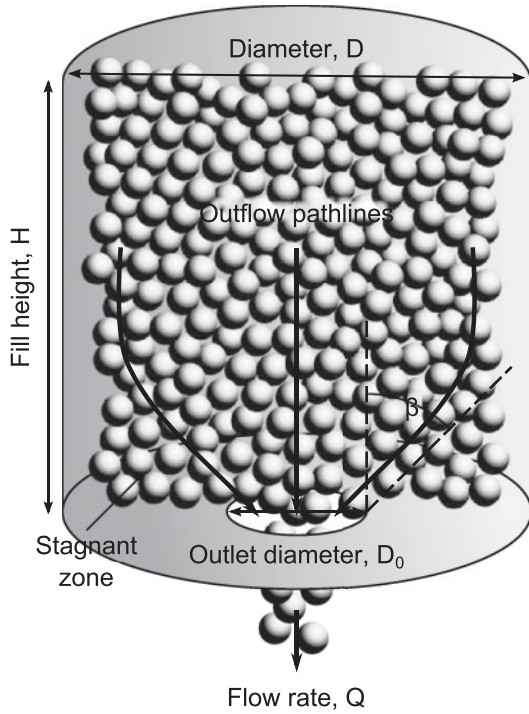
FIG. 1. Schematic diagram for discharge from a cylindrical flat-based hopper with fill height H, diameter D, outlet diameter D_0, and particle diameter d. Particles form a flowing cone with slope angle β over a slowly moving, almost stagnant, zone within the hopper.

Fig. 2(a). The concept of this "free-fall arch" has been used in many theoretical analyses [5].

Equation (1) agrees well with experimental flow rates for particle diameters down to $O(\sim 100\,\mu\text{m})$. For smaller particles
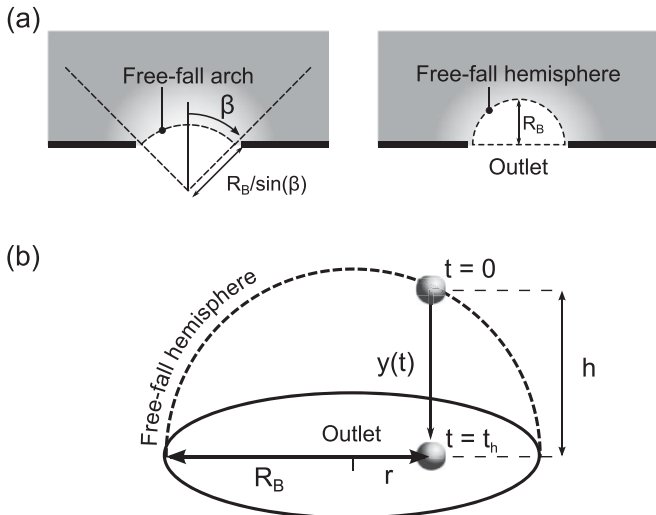

FIG. 2. (a) Difference between vertical cross sections through the free-fall domain in previous analyses (left), where the region is assumed to be a spherical section, and our approach (right), where it is assumed to be a hemispherical region. Previous analyses have also determined the flow rate from integration over a conical section (left). (b) The free-fall domain used in our analysis. Particles leave the free-fall hemisphere and fall a distance h to the outlet. The time taken for the particle to reach the outlet is t_h.

the flow-impeding effects of gas drag on the particles cannot be neglected, leading to a significant deviation between Eq. (1) and experimental results. Expressions for the outflow rate where the effect of gas drag is included are much more difficult to determine. A common approach used in many previous methods is an ad-hoc modification of Eq. (1) with the addition of a pressure gradient opposing gravity to give a modified relation of the form

$$Q = C\rho_b \sqrt{D_B^5 \left(g + \frac{1}{\rho_b} \frac{\partial p}{\partial r} \right)}, \qquad (2)$$

where the pressure gradient is determined from the Carman-Kozeny equation:

$$\frac{\partial p}{\partial r} = -\frac{K\eta}{d^2} \left(\frac{1 - \epsilon}{\epsilon_b} \right)^2 u_r, \qquad (3)$$

where K is the empirical Carman-Kozeny constant, $K \simeq 180$, and the relative velocity u_r is given by $u_r = u - v$, where u is the gas velocity and v is the averaged particle velocity over the region where the expression is used. This approach relies on the assumption that the outflowing particles in the vicinity of the outlet can be treated as a porous medium, disregarding the discrete nature of the particles. An approach used by Crewdson [8] derived an expression for the slip velocity in terms of the flow rate from a sequence of assumptions regarding the voidage distribution and stresses within the bed. A Taylor expansion was used for terms involving powers of $(1 - \epsilon)/\epsilon$ in the Carman-Kozeny equation, and an empirical substitution for the stress was used to derive an approximate value of the voidage over the outlet. The stress term overpredicts the stress at the outlet and the voidage term overpredicts the voidage, but the assumption was made that both errors compensate to give a correct result. The resulting expression for the flow rate, in terms of the constant C in Eq. (1), is given by

$$C = \sqrt{\rho_b^2 g - \frac{2QK\eta(1 - \epsilon_b)}{\pi\epsilon_b^2 d^2 D_0^2 (1 - \cos\beta)[\epsilon_b(1 - \epsilon_b) + c(3 - \epsilon_b)]}}, \qquad (4)$$

where c is an empirical compressibility index. A quadratic equation was given for determining the flow rate Q from Eq. (4).

An alternative method for modeling the system is to formulate the granular dynamics in an equivalent thermodynamic context. This approach was introduced and used by Brown [9] to derive the outflow rate by assuming the total mechanical energy per unit mass decreases along a flow streamline until it is minimized at the free-fall arch. This method was extended by Altenkirch to incorporate interstitial gas effects by assuming friction can be neglected in the dilute region and forces due to interstitial pressure gradients dominate [10]. The gas and solid volume flow functions are assumed to be linearly related, giving the relative gas-particle velocity u_r as

$$u_r = \left(1 - \alpha \frac{1 - \epsilon}{\epsilon_b} \right) y'(t), \qquad (5)$$

where α is the ratio of gas to solid volume flow rates and primes represent a derivative with respect to time, $\partial/\partial t$, such that $y'(t)$ is the particle velocity. The pressure gradient from

the Carman-Kozeny equation (3), was also used in the analysis. The discharge flow rate is calculated by integration of the radial flow field over a cone of angle β, as shown in Fig. 2(a). This gives the flow rate constant C in Eq. (1) as

$$C = \frac{\pi}{6} \left(\frac{(\gamma^2 + 1)^{\frac{3}{2}} - (\gamma^2 + \cos\beta)^{\frac{3}{2}} + \frac{3}{2}\gamma(\cos\beta - 1)}{\sin^{\frac{5}{2}}\beta} \right),$$

(6)

where

$$\gamma = \frac{\sqrt{D_0}}{4\rho_b\sqrt{g}} \frac{K\eta}{d^2} \left(\frac{1 - \epsilon_b}{\epsilon_b} \right)^2 \left(1 - \alpha\frac{1 - \epsilon_b}{\epsilon_b} \right).$$

(7)

Many previous hopper flow analyses have used a conical flow domain of this type for determining the outflow rate [8–14]. For flat-based hoppers, such as the ones used in this study, β is usually assumed to be $\beta = 45°$ in the absence of further information [15]. The mass flow rate is therefore a function of the empirical parameter K and the flow ratio α. For sealed hoppers, gas flow only occurs through the outlet [10]. In this case, the volume flow rates must be equal and opposite at the hopper outlet, giving $\alpha = -1$. This assumption is only valid within the hopper as we show α switches sign just below the outlet, making it unsuitable for conical domains of integration, which extend beyond this region. Expressions for α have been derived from models of the voidage variation within the free-fall region [13], although in our analysis α is assumed constant as we only consider the region within a sealed hopper.

The pressure gradient within the hopper can also be measured experimentally from the pressure difference Δp between two points within the hopper, giving a relation of the form

$$C = K_1\sqrt{g + K_2\Delta p},$$

(8)

where K_1 and K_2 are empirical constants [16]. A variety of related expressions have been given [17–19]. The majority of models for hopper flow incorporating the effects of interstitial gas follow a similar approach, with an ad-hoc pressure gradient being added to reduce the effect of the gravitational term. We show that this approach is unnecessary, as the flow rate can be derived directly by integration of the particle velocity distribution at the hopper outlet. Our analysis relies on no empirical expression for the stress distribution within the hopper, or on the addition of a Carman-Kozeny term.

II. DERIVATION OF FLOW RATES FOR A CYLINDRICAL FLAT-BASED HOPPER

A. Flow rates without gas drag

The empirical expression for hopper discharge rate, Eq. (1), can be derived by integrating the velocity of the discharging particles over a hemisphere spanning the outlet. This approach differs from previous approaches by assuming the free-fall region is hemispherical and starts from the base of the hopper, rather than a cone of angle β projecting upward from below the center of the outlet, as shown in Fig. 2(a). A hemispherical domain of integration resolves the problem of a singularity at the apex of a conical integration region as $r \to 0$. Furthermore, the mass flux is assumed to be perpendicular to the outlet in

our analysis, which conforms better to observations than the assumption of a conical-shaped flow field below the outlet of the hopper.

The particles are assumed to fall from the surface of the hemisphere freely under gravity. The flow rate is measured as the mass flux through the horizontal plane of the outlet. The vertical distance, h, each particle falls from the hemisphere to the outlet plane is dependent on the radial position, r, of the particle. This is given by $h(r) = \sqrt{R_B{}^2 - r^2}$, as shown in Fig. 2(b). The particles are reasonably assumed to have a negligible velocity on the hemisphere, compared to their final outflow velocity. The flow rate over the outlet plane is then given by

$$Q = 2\pi\rho_b \int_0^{R_B} r\, y'(t_h, r)\, dr,$$

(9)

where t_h is the time it takes a particle to vertically fall a distance h and cross the horizontal plane of the outlet. No assumptions regarding the geometry are required in the analysis, with the exception of the reduced diameter, D_B, as this is a physical effect due to particle clustering around the orifice.

The equation of motion with initial conditions for a single particle falling from rest with no gas drag and no collisional interactions is

$$y''(t) = g, \quad y'(0) = 0$$

(10)

with the trivial solution

$$y(t) = \tfrac{1}{2}gt^2,$$

(11)

$$y'(t) = gt.$$

(12)

Solving Eq. (11) for t_h at $y = h$ and substituting into Eq. (12) gives

$$y'(t_h, r) = \sqrt{2g}\left(R_B^2 - r^2\right)^{\frac{1}{4}}.$$

(13)

Substituting this into the flow rate integral, Eq. (9), gives the flow rate as

$$Q = \frac{\pi}{5}\rho_b\sqrt{gD_B^5},$$

(14)

which is Beverloo's relation, Eq. (1), with $C = \pi/5 = 0.628$, well within the empirically measured range [5]. The change in the conceptual shape used makes the analysis particularly simple and allows the Beverloo expression to be derived without the use of assumptions that restrict the range of validity of the relationship.

B. Flow rates incorporating the effects of gas drag

This analysis can be extended to account for the effects of gas drag on the particles. Due to the low particle Reynolds number at the small length scale where drag dominates, the drag force, F_d, on each particle is Stokesian:

$$F_d = -3\pi d\eta u_r,$$

(15)

where η is the gas viscosity. Using Eq. (5) for the relative gas velocity gives

$$F_d = -3\pi d\left(1 - \alpha\frac{1 - \epsilon}{\epsilon}\right)\eta y'(t),$$

(16)

where α is the ratio of gas to solid flow rates, Eq. (5). The resulting equation of motion with initial conditions for each particle is

$$y''(t) = g - \left(1 - \alpha\frac{1 - \epsilon_b}{\epsilon_b}\right)\frac{18\eta}{\rho_p d^2}y'(t), \quad y'(0) = 0, \quad (17)$$

where the bulk voidage fraction, ϵ_b, has been assumed constant over the free-fall region. To simplify the analysis, two time scales are introduced: the inertial time scale,

$$\tau_i = \sqrt{\frac{R_B}{g}}, \quad (18)$$

and the viscous time scale,

$$\tau_\eta = \left(1 - \alpha\frac{1 - \epsilon_b}{\epsilon_b}\right)^{-1}\frac{\rho_p d^2}{18\eta}. \quad (19)$$

The use of these two time scales allows Eq. (17) to be cast in a particularly simple form as

$$\bar{y}''(\bar{t}) = k[1 - \bar{y}'(\bar{t})], \quad \bar{y}'(0) = 0, \quad (20)$$

where the overbars represent nondimensionalized variables and $k = (\tau_i/\tau_\eta)^2$. The Stokes number, St, is the ratio of viscous to inertial time scales in the system, so k is related to the Stokes number by $k = 1/\text{St}^2$. For St $\gg 1$, the granular motion is inertially dominated, whereas viscous drag dominates at St $\ll 1$.

The solution of Eq. (20) is

$$\bar{y}(\bar{t}) = \frac{1}{k}(e^{-k\bar{t}} - 1) + \bar{t}, \quad (21)$$

$$\bar{y}'(\bar{t}) = 1 - e^{-k\bar{t}}. \quad (22)$$

Solving Eq. (21) for $\bar{t}_h$ at $\bar{y} = \bar{h}$ gives

$$\bar{t}_h = \frac{1}{k}[1 + k\bar{h} + W(-e^{-k\bar{h}-1})], \quad (23)$$

where W is the Lambert-W function, defined as $x = W(x)e^{W(x)}$, and $\bar{h}(\bar{r}) = \sqrt{1 - \bar{r}^2}$, $\bar{r} = \frac{r}{R_B}$. The Lambert-W function commonly occurs in solution to differential equations of this type, and the range used here is restricted to the upper branch between $W(0) = 0$ and $W(-e^{-1}) = -1$. It cannot be expressed in terms of elementary functions, but several accurate approximations for this branch exist, given in terms of logarithms [20,21]. Substituting this into the expression for $\bar{y}'$, Eq. (22) gives the particle velocity at the outflow plane as

$$\bar{y}'(\bar{t}_h, \bar{r}) = 1 + W(-e^{-k\sqrt{1-\bar{r}^2}-1}), \quad (24)$$

where the definition of the Lambert-W function has been used to simplify the result. The dimensionalized flow rate can then be found by using Eq. (9):

$$Q = \pi\rho_b R_B^2\tau_\eta g\left[1 + 2\int_0^1\bar{r}W(-e^{-k\bar{h}-1})\,d\bar{r}\right]. \quad (25)$$

This can be solved in closed form to give an expression for the flow rate incorporating the effects of interstitial
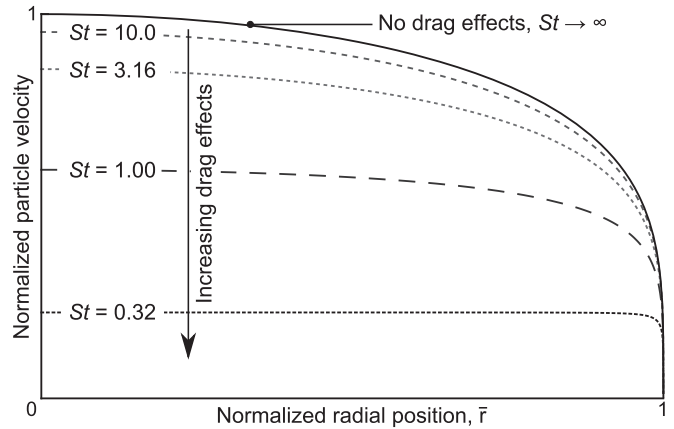

FIG. 3. Difference in nondimensionalized velocity profiles with and without drag effects, Eqs. (24) and (13) (nondimensionalized), respectively. At large Stokes numbers, inertial terms dominate and the profiles are the same. Around St $\sim$ 10, the profiles diverge, with drag effects causing a plug profile. Low Stokes numbers give a broader and flatter plug profile.

gas:

$$Q = \pi\rho_b R_B^2\tau_\eta g\left[1 + \frac{1}{k^2}\left(\frac{5}{6} + \frac{w_k^2}{6}(2w_k + 3)\right.\right.$$
$$\left.\left. + w_k(w_k + 2)(k + 1)\right)\right], \quad (26)$$

where

$$w_k = W(-e^{-k-1}). \quad (27)$$

The closed-form result must be evaluated with high numerical accuracy at large length scales, so we directly evaluate Eq. (25) numerically for the comparisons used within this study.

The difference in predicted nondimensionalized particle velocity profiles at the outlet without gas and including gas drag effects, Eq. (24), is shown in Fig. 3. The expression for the profile with no drag, Eq. (13), is nondimensionalized to $\bar{y}'(\bar{r}) = \sqrt{2k}(1 - \bar{r}^2)^{\frac{1}{4}}$, so all plots have been normalized by dividing by $\sqrt{2k}$. The plot is shown in terms of the Stokes number, St $= 1/\sqrt{k}$. As St $\to \infty$, the velocity profile converges to that of the profile for flow with no drag effects. Below St $\sim$ 10, the velocity profiles diverge, with the inclusion of drag effects giving a plug flow profile. This profile becomes broader and flatter as St decreases, where the limiting form at $k \to 0$ is a flat profile over the entire outlet.

At small particle diameter, viscous effects will dominate and the particles will fall at a terminal velocity, y_t'. From Eq. (15), and using the assumption that the particle density is much greater than the gas density, this is $y_t' = \tau_\eta g$. The outflow rate for particles at terminal velocity, Q_t, can be determined by using this expression in Eq. (9) to give

$$Q_t = \pi\rho_b R_B^2\tau_\eta g. \quad (28)$$

From inspection, it can be seen that Eq. (28) is equal to the left-hand side of Eq. (25), and the integral term in Eq. (25), therefore, represents an inertial correction to the viscous limit of the flow rate.

III. COMPUTATIONAL MODELING OF HOPPER DISCHARGE

To test the derived theoretical expressions for the flow rates, Eqs. (14) and (25), the discharge of hoppers at a range of length scales spanning several orders of magnitude must be measured. Ideally, the geometry and particle setup must be the same in each test so that any differences in flow rate are due only to the effect of the length scale alone. This is difficult in practice, but straightforward using computational modeling.

We use a Lagrangian approach for particles called the discrete element method (DEM), which was first formulated by Cundall and Strack [22]. Hopper flow has been investigated extensively computationally using the DEM. Potapov and Campbell carried out one of the first investigations into hopper discharge using the DEM [23]. Later, Holst *et al.* carried out a detailed range of simulations on silo filling to compare continuum and DEM models [24]. Recent studies include that of Zhu and Yu [25], who investigated the dependency of solids mass flow rate on orifice diameter using a flat-based cylindrical geometry scaled by a fixed particle diameter. The simulation results correlated well with the Beverloo equation. Anand *et al.* [15] utilized the DEM to investigate the dependence of mass flow rate on particle properties in a pseudo-three-dimensional angled hopper. The majority of DEM simulations assume spherical particle geometry, however Cleary and Sawley [7] have shown that particle shape can significantly alter hopper mass flow rates. Using a superquadric formulation, it was found that particles of large aspect ratio give a flow rate reduction of up to 30% over spherical particles. Sphero-disks [26] and spherical clusters [27] have also been considered. Applying shear to the base of the hopper through rotation has also been shown to cause an increase in the hopper outflow rate [28].

The effect of gas flow on hopper discharge has, however, been largely neglected. Eulerian-Lagrangian coupling of gas and solid phases was introduced to the DEM by Tsuji *et al.* [29] in the context of two-dimensional fluidized beds. Langston *et al.* [30] investigated the effects of drag on particle flow rate in a shallow angled hopper for closed-top gravity flow and open-top air-assisted discharge. For the closed-top case, solids flow rates were observed to decrease with decreasing effective particle density. For the air-assisted case, an increase in the forcing overpressure led to a steady increase in particle velocity magnitudes and increasing wall stresses. A solid discharge ratio from air-assisted simulation data was compared to a continuum result of Nedderman [31], although no comparison to theoretical correlations concerning the effect of particle size scale on gas-drag effects was presented. The assumption of radial gas flow was used, and interstitial fluid effects were modeled by varying the effective particle density. More recently, Guo *et al.* [32] used the DEM to investigate the effects of interstitial gas drag on fine particles in die-filling. A pseudo-two-dimensional flat-based geometry was used, and both particle diameter and density were varied systematically. For vacuum conditions, simulation results for monodisperse particles were observed to have an average dimensionless flow rate agreeing well with the Beverloo expression, Eq. (1). Small particle diameters and low densities both gave a lower mass flow rate when a gas model was used.

The DEM model used in our simulations and the details of the particle coupling to the gas field are given in the following sections.

A. Particle dynamics

The computation and time integration of the forces and velocities for a large set of individual particles forms the basis of the DEM. In this implementation, the particle-particle contact force, $\mathbf{F}_c$, is determined by the particle overlap information using a linear spring, dashpot and slider approximation. This force is the sum of a normal force $\mathbf{F}_n$ and a tangential force $\mathbf{F}_t$ at the contact point. The normal force is determined from the particle overlap $\delta\mathbf{l}$ and relative normal velocity $\mathbf{v}_n$:

$$\mathbf{F}_n = -k_n\delta\mathbf{l} + C_n\mathbf{v}_n, \tag{29}$$

where C_n is the normal damping coefficient, chosen to give the required normal coefficient of restitution, and k_n is the spring stiffness. The spring stiffness determines the maximum particle overlap, which is $\sim 0.1\%$ of the particle diameter, to give an accurate simulation within a reasonable computational time frame.

The tangential force is determined incrementally by calculating

$$\delta\mathbf{F}_t = (k_t\delta t + C_t)\mathbf{v}_t, \tag{30}$$

where k_t is the tangential spring stiffness, δt is the integration time step, C_t is the tangential damping coefficient, and $\mathbf{v}_t$ is the relative tangential surface velocity. The tangential force is then updated with this increment if the new tangential force does not exceed the Coulomb friction limit:

$$\mathbf{F}_t^{\text{new}} = \begin{cases} \mathbf{F_t} + \delta\mathbf{F_t} & \text{if} \quad \mathbf{F}_t + \delta\mathbf{F_t} < \mu\mathbf{F}_n, \\ \mu\mathbf{F}_n & \text{otherwise}, \end{cases} \tag{31}$$

where $\mathbf{F}_t^{\text{new}}$ is the tangential force at the next time step and μ is the interparticle coefficient of friction.

The force balance on each particle i is given by

$$m_i\frac{d\mathbf{v}_i}{dt} = \mathbf{F}_{ci} + \mathbf{F}_{gi} + m_i\mathbf{g}, \tag{32}$$

where m_i is the mass of particle i and $\mathbf{v}_i$ is the velocity. The forces consist of the solid particle-particle contact force, $\mathbf{F}_c$, a gas-particle interaction force, $\mathbf{F}_g$, and the gravitational force $m\mathbf{g}$. The gas-particle interaction force, $\mathbf{F}_g$, is the sum of the gradient of the gas pressure, p, and the particle drag force, $\mathbf{F}_d$:

$$\mathbf{F}_{gi} = -V_i\nabla p + \mathbf{F}_{di}, \tag{33}$$

where V_i is the particle volume. The moment balance on each particle is given by

$$I_i\frac{d\boldsymbol{\omega}_i}{dt} = \mathbf{T}_i + \mathbf{T}_{di}, \tag{34}$$

where I_i is the moment of inertia in the principal frame of the particle, $\mathbf{T}_i$ is the interparticle contact torque, $\mathbf{T}_{di}$ is a Stokesian rotational drag on the particle, and $\boldsymbol{\omega}_i$ is the spin of the particle.

The dominant gas-particle interaction is the drag force on each particle. Other gas-particle interaction forces such as the Saffman shear lift force, the Magnus rotational lift force, and the Basset force are considered small enough to be neglected

in this system. The drag force exerted by the gas on a single particle must be corrected in multiparticle systems to account for the presence of neighboring particles. We use an empirical correction given by Di Felice [33]:

$$\mathbf{F}_{di} = \tfrac{1}{2} C_d \rho_g \epsilon^{-\chi} A_\perp |\mathbf{u}_r|^2 \mathbf{u}_r,$$ (35)

where χ is given by

$$\chi = 3.7 - 0.65 \exp\left[-\frac{(1.5 - \log \mathrm{Re})^2}{2}\right]$$ (36)

and the particle Reynolds number, Re, for a particle of diameter d in a gas with viscosity η is $\mathrm{Re}_p = d\rho_g|\mathbf{u}_r|/\eta$. We use a drag coefficient given by Holzer *et al.* [34] for spherical particles:

$$C_d = \frac{27}{\mathrm{Re}} + 0.42.$$ (37)

Particles are also subject to Stokesian rotational drag, given by

$$\mathbf{T}_d = \pi \eta d^3 \boldsymbol{\omega}_r,$$ (38)

where $\omega_\mathbf{r}$ is the particle rotation vector relative to the fluid, given by $\boldsymbol{\omega}_r = \tfrac{1}{2}\boldsymbol{\omega}_g - \boldsymbol{\omega}_p$, $\boldsymbol{\omega}_g$ is the curl of the gas velocity field, and $\boldsymbol{\omega}_p$ is the spin of the particle.

B. Fluid dynamics

The constitutive equations for gas flow through a particle bed are derived by Anderson and Jackson [35], and are given by Kafui [36] in a "pressure gradient force" (PGF) form. These can be reformulated into relations for a superficial gas velocity, $\mathbf{u}'$, rather than an interstitial gas velocity, $\mathbf{u}$, using $\mathbf{u}' = \epsilon \mathbf{u}$ and making the assumption that the gas density, ρ_g, is constant, giving

$$\frac{\partial \epsilon}{\partial t} = -\boldsymbol{\nabla} \cdot \mathbf{u}'$$ (39)

$$\frac{\partial \mathbf{u}'}{\partial t} + \frac{1}{\epsilon}(\mathbf{u}' \cdot \boldsymbol{\nabla})\mathbf{u}' + \mathbf{u}' \boldsymbol{\nabla} \cdot \left(\frac{\mathbf{u}'}{\epsilon}\right)$$
$$= -\frac{\epsilon \boldsymbol{\nabla} p}{\rho_g} - \frac{\mathbf{f}_g}{\rho_g} + \frac{\boldsymbol{\nabla} \cdot (\epsilon \boldsymbol{\tau}')}{\rho_g} + \epsilon \mathbf{g},$$ (40)

where p is the pressure and $\boldsymbol{\tau}'$ is the local stress tensor, given by

$$\boldsymbol{\tau}' = \eta \left(\boldsymbol{\nabla} \frac{\mathbf{u}'}{\epsilon} + \boldsymbol{\nabla} \frac{\mathbf{u}'^T}{\epsilon}\right).$$ (41)

Due to the moderate Reynolds numbers over the system considered here ($< 10^3$), no turbulence terms are included in our simulations. The particle-gas interaction body force, $\mathbf{f}_g$, is defined as

$$\mathbf{f}_g = \frac{1}{V_c} \sum_{i=1}^{n_c} \mathbf{F}_{di} = \frac{1}{V_c} \sum_{i=1}^{n_c} \frac{1}{2} \rho_g |\mathbf{u} - \mathbf{v}_i|$$
$$\times C_d A_\perp \epsilon^{(2-\chi)} (\mathbf{u} - \mathbf{v}_i),$$ (42)

where n_c is the number of particles in the characteristic gas volume V_c.

The gas flow is numerically calculated using a modification of the pressure correction method, using Eq. (39) as a source term [37]. This method is more straightforward than methods based on compressible flow equations, which require an extra expression for the energy term as well as an equation of state. The equations are discretized onto a semistaggered grid to reduce checkerboard pressure oscillations, with velocity and force defined on the cell vertices, and voidage fraction, pressure, and the stress tensor defined at the cell centers. Advection terms are calculated using upwind biased methods and divergence; curl and gradient terms are calculated using semi-staggered finite-difference stencils. The forces on the gas from the particles are mapped using collocation, whereas the forces from the gas on the particles are mapped using trilinear interpolation. The effect of the hopper geometry on the gas solution is implemented by imposing a zero-velocity no-slip condition on computational cells intersecting with any solid boundaries. Time integration is carried out using a second-order Runge-Kutta method. This method has been validated for a range of gas-particle flows, including fluidized beds [37] and pneumatic conveying systems [38].

IV. EFFECT OF SCALING

To allow us to determine the effects of interstitial gas at different length scales, two sets of simulations were carried out at a range of length scales, one with gas effects and the second in vacuum. Each simulation used the same particle setup, so that any differences between the simulations were due only to the imposed scaling. The base setup was $H = 6.0$ m, $D_0 = 1.0$ m, $D = 3.0$ m, and $d = 62.5$ mm ($= D_0/16$), containing around $\sim 200\,000$ particles for a closed-top hopper. The dimensions were chosen to ensure that the bed filling height and the ratio of particle diameter to orifice diameter did not affect the particle outflow rate. The grid resolution was $16 \times 62 \times 16$, giving a cell size of 200 mm and a ratio of cell to particle diameter of 3.2. The mass flow during discharge rapidly reaches steady state, where it remains until the hopper has almost emptied. The flow rate was measured through the plane 1 m vertically below the orifice. This base setup was run over a range of length scalings, s, given in Table I. This scaling was applied to all parameters in the simulation that were dependent on length, including the spring constant k. The parameters used in the simulation are given in

TABLE I. Size scalings used in simulations.

Scaling factor, s	Particle diameter, d
1.0	62.5 mm
1.0×10^{-1}	6.25 mm
1.0×10^{-2}	625 μm
5.0×10^{-3}	312.5 μm
2.5×10^{-3}	156.25 μm
1.0×10^{-3}	62.5 μm
7.5×10^{-4}	46.875 μm
5.0×10^{-4}	31.25 μm
2.5×10^{-4}	15.625 μm
1.0×10^{-4}	6.25 μm

TABLE II. Simulation parameters.

Name	Symbol	Values
Carman-Kozeny coefficient	K	180
Angle of stagnant region	β	$\pi/4$
Beverloo diameter constant	k	1.5
Gravity magnitude	g	9.8 m/s^{-2}
Gas viscosity	η	1.8×10^{-5} Pa s
Particle friction	μ	0.3
Gas density	ρ_g	1.2 kg/m^3
Particle density	ρ_p	2700 kg/m^3
Voidage fraction (free-fall region)	ϵ_b	0.44

Table II, along with the constants used in the theoretical models. The average bulk density within the free-fall hemisphere was used for ϵ_b, as per Kotchanova's suggestion [6]. This is difficult to measure experimentally but straightforward in our computational simulations.

Figure 4 shows hopper discharge at five different hopper scalings. Particle sizes of $d = 62.5$ mm and $d = 6.25$ mm discharge as a linear stream, where the width of the stream $\sim D_B$. For these particle sizes, the interstitial gas has a negligible effect on the flow rate. For $d = 625$ μm particles, slight sinuations appear in the discharge stream, showing gas effects beginning to affect the outflow. These are much more evident at $d = 62.5$ μm, where a kink in the path can clearly be seen midway down the stream. The stream is also slightly pinched at the bottom, where the width of the stream $< D_B$. The gas effects can very clearly be seen in the smallest length scale considered, with $d = 6.25$ μm particles. The stream here is pinched and clumped, with a correspondingly large decrease in flow rate. This effect has been experimentally observed and investigated [39].

The behavior of the gas within the free-fall region is crucial to the dynamics of the particles during discharge. Figure 5 shows gas velocity streamlines in the vicinity of the outlet. There is an annular backflow of gas into the hopper around the
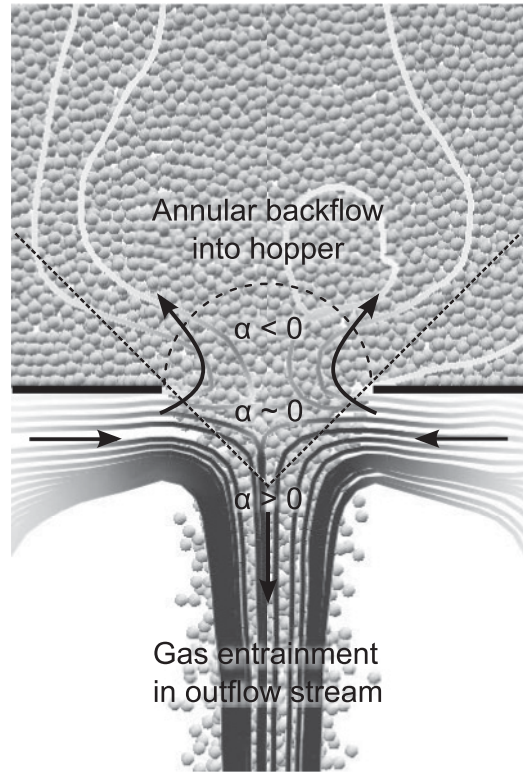

FIG. 5. Gas velocity streamlines near the hopper outlet, shaded by velocity magnitude, superimposed over the discharging particles. The base of the hopper is shown as the two thick horizontal lines, and the average gas flow direction is schematically indicated by the arrows. Gas is drawn into the hopper through an annular region just inside the rim of the outlet. The velocity of the gas just below the center of the outlet is close to zero. Further below the outlet gas is entrained by the discharging particles.

outside of the outlet that percolates upward through the hopper bed. Along the central axis of the hopper, within the free-fall hemisphere, the gas flow is in the opposite direction to the
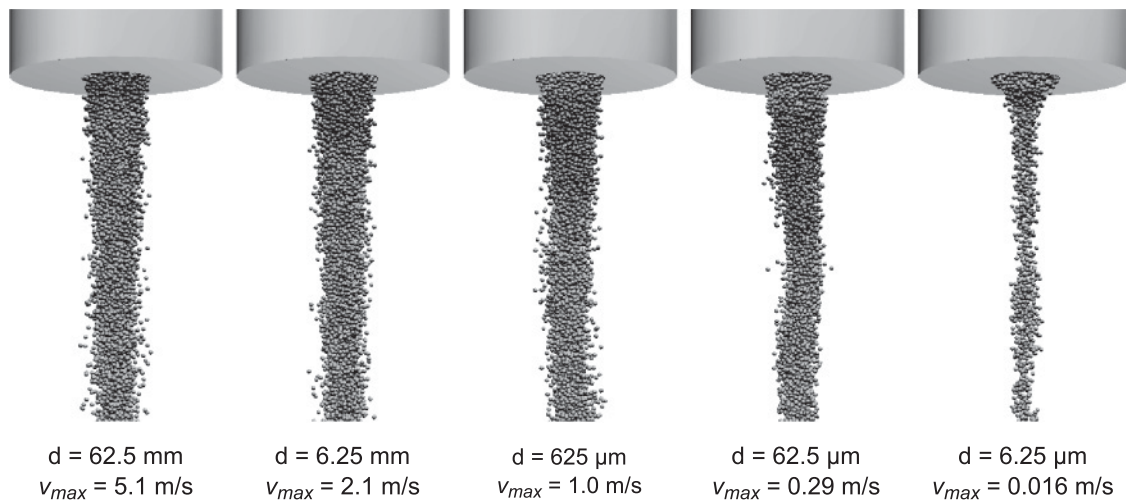

FIG. 4. Outflow from five hoppers with scaling ranging from $D_0 = 1.0$ m to $D_0 = 0.1$ mm. Each image has been scaled for comparison. The maximum particle velocity, v_{max}, is reached at the base of the particle stream. Gas drag can be seen altering the outflow path in the $d = 625$ and 62.5 μm cases. The effects of the interstitial gas are most apparent in the $d = 6.25$ μm scaling case with pinching of the stream.
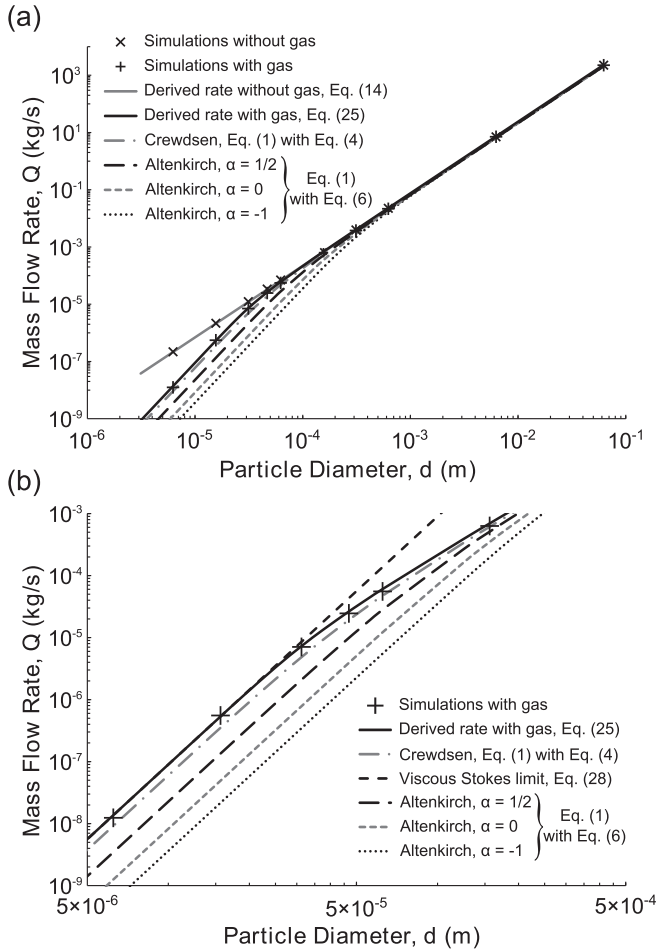
FIG. 6. Logarithmic plot of simulation and theoretical flow rates, (a) in vacuum and gas and (b) in gas only. The flow rates in vacuum closely match the Beverloo relation, Eq. (1), with $C = \pi/5$, as given by Eq. (14). The flow rates incorporating gas effects very closely match the derived expression, Eq. (25). Equation (6) is shown for three values of α. All overpredict the drag and therefore underpredict the flow rates at small length scales.

motion of the particles. The volume flux must balance within the hopper, so the ratio of gas to solid volume flow rates, α, within this region gives $\alpha = -1$. Just below the outlet, the gas flow is almost stationary, balanced by the pressure drop from the discharging hopper above and the downstream entrainment of the gas below, giving $\alpha \sim 0$. Further below the outlet, the gas is strongly entrained by the falling particles and the gas flow is in the same direction as the particle flow, giving $\alpha > 0$.

The steady-state flow rates at each scaling are shown in Fig. 6 on a logarithmic plot. The results in vacuum are plotted with Eq. (1), where $C = \pi/5$, as given by Eq. (14). Our results very closely match Eq. (1) for flow rates with no gas, showing that the empirical prefactor in this relation is purely dependent on the geometry of the free-fall region within the hopper. The results incorporating the effects of interstitial gas are also plotted with the new theoretical expression, Eq. (25). The value of α has been taken to be $\alpha = -1$. Equation (25) closely matches the simulation flow rates across the full range of scales. At very small particle diameters, with correspondingly low Stokes numbers, the particles fall at a terminal velocity.

From Eq. (28), the outflow rate at this terminal velocity $Q_t \sim d^4$ in this system, as $D_B \sim d$ and $\tau_\eta \sim d^2$. Figure 6(b) shows that the simulation and theoretical flow rates obey this dependency on d^4 and approach Q_t in the low Stokes number limit, as expected.

The flow rates from previous models are also plotted in Fig. 6, where C in Eq. (1) is given by Crewdsen's expression, Eq. (4), and Altenkirch's expression, Eq. (6). The flow rates from the simulations match Eq. (4), but show a mild sensitivity to the empirical compressibility parameter c. The parameter c is taken as $c = 0.025$, which was chosen as the closest corresponding value to the measured bulk density in the simulation from a set of values given by Crewdsen [8]. Equation (6) is plotted for three values of α but greatly overpredicts the effect of gas drag for each of these. This difference is due to the value of α used in the derivation of Eq. (6), which was assumed to be a constant value over the entire conical integration region used in the analysis [10]. This is clearly not the case, as this conical region extends beneath the outlet, and the sign of α switches from the top to the bottom of this region. In contrast, our analysis uses the value $\alpha = -1$ only within the hopper, which is exact as it is a sealed system.

Our theoretical expression for the flow rate, Eq. (25), does not rely on assumptions for the gas flow, and hence the value of α, outside the hopper. No assumptions are also made regarding the stress distribution within the granular material, such as the angle of repose in the hopper $\beta = 45°$. Furthermore, the model does not rely on approximations of the pressure field within the bed, such as the Carman-Kozeny equation. The derived expression closely matches our simulation data without requiring any additional parameters.

Figure 6 shows that two regimes exist for the flow rates incorporating gas effects: an inertial regime at large particle diameters, with a flow rate $Q \sim d^{\frac{5}{2}}$, and a viscous drag-dominated regime, with a flow rate $Q \sim d^4$, at small particle diameters. The transition between these two regimes occurs at a critical Stokes number, which can be determined from the point of divergence between the flow rates with and without gas. Figure 7 shows a plot of the ratio of these flow rates against the Stokes number. The transition occurs where this ratio diverges from unity, around St ~ 10. A related study
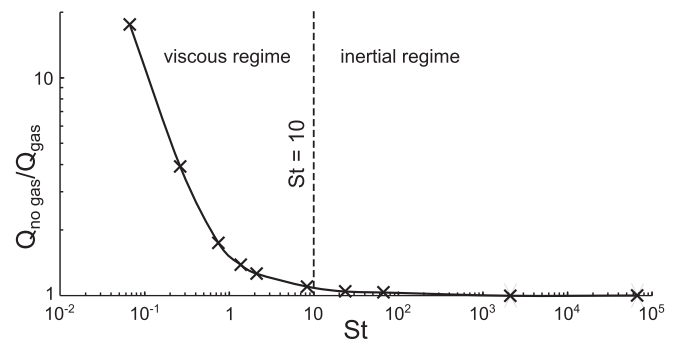

FIG. 7. Ratio of simulation flow rates in vacuum and gas, plotted against the Stokes number on a logarithmic scale. The transition from inertial to viscous dominated granular dynamics occurs where the ratio diverges from unity, around St ~ 10, shown as a vertical dashed line.

of granular avalanches in gases and fluids gave the same value for the transitional Stokes number [40], showing that this critical value appears to apply over a range of coupled gas-grain systems.

V. CONCLUSION

Expressions for outflow rates from a flat-based hopper have been derived by integration of the mass flux of freely falling particles over a hemispherical region just within the hopper. In contrast to previous models, our method is based on the motion of the individual particles, rather than a flow rate expression derived from dimensional arguments. Previous models have also typically relied on integration using spherical coordinates over a conical region matching an arbitrarily imposed funnel-shaped discharge region within the hopper. A conical region of integration implies that the particle flow at the outlet is directed toward the apex of this cone, which is not observed to be the case. The new model assumes outflow perpendicular to the outlet, which matches observations. Furthermore, the model imposes no arbitrary conditions on the granular material within the hopper, such as a funnel-shaped discharge region, giving a broad range of applicability to similar systems.

For the case in which the effects of interstitial gas are neglected, the new expression for the flow rate, Eq. (14), is identical in form to the empirical Beverloo relation, Eq. (1). Comparison of the terms between these relations shows that the empirical constant used in Eq. (1) results from the geometry of the integration region. The new analysis derives this empirical expression purely by considering the motion of the individual particles.

At low Stokes numbers, the discharge rates strongly deviate from Eq. (14) due to drag from the interstitial gas. The analysis was extended to take this into account by incorporating a drag relation into the expression for the motion of the individual particles. When drag is taken into account, the particle velocity has a functional form dependent on the upper branch of the Lambert-W function, Eq. (24). The bulk flow velocity of small particles, experiencing high drag, takes the form of a plug-shaped profile over the outlet, as shown in Fig. 3. This plug flow profile gives the corresponding decrease in mass flow rate observed at small particle length scales.

The decrease in flow rate occurs at the transition between the inertial and viscous dominated regimes of particle motion. The critical Stokes number at the point of transition in this system was found to be St $\sim$ 10. This is the same value found in previous studies of related gas-particle systems [40]. As St $\to \infty$, the system is inertially dominated, the interstitial gas has a negligible effect on the flow rate, and Eq. (14) can be used. As St $\to 0$, the system is dominated by viscous drag effects, the hopper outflow rate decreases, and our expression taking the interstitial gas into account, Eq. (25), applies.

The new flow rate expressions have been compared to computational results from a coupled gas and DEM model. The derived flow rates with and without interstitial gas effects both very closely match the flow rates measured from the simulations over a range of length scales. Earlier empirical and semiempirical models for the flow rate were also compared to the simulation results. The Crewdsen relation, Eq. (1), with C given by Eq. (4), slightly underpredicts the flow rates and also depends on an empirically determined compressibility parameter. The Altenkirch relation, Eq. (1), with C given by Eq. (6), was found to perform poorly, underpredicting the flow rate over a range of α. The simulations allowed us to examine the gas flow field in the vicinity of the outflow, showing that gas flow reverses direction just under the outlet. The value of α was assumed constant in the derivation of Eq. (6), but changes sign over the hemispherical domain of integration used in this analysis. This assumption was shown only to hold within the domain used in our analysis.

The close match between the derived flow rates and the simulations shows that the new theoretical model accounts for the diverse range of dynamics within this granular system. Our analysis shows that the discharge flow rate from a sealed flat-based hopper, with spherical particles, can be derived from a straightforward relation integrated over a hemispherical region, requiring no empirical or fitting parameters. The methodology leading to the derivation of the flow profiles may also have a wide range of additional applications in related gas-grain systems.

[1] M. S. Ketchum, *The Design of Walls, Bins and Grain Elevators* (McGraw-Hill, New York, 1929).

[2] R. L. Brown and J. C. Richards, Trans. Inst. Chem. Eng. Chem. Eng. **38**, 243 (1960).

[3] M. Sperl, Granular Matter **8**, 59 (2006).

[4] W. A. Beverloo, H. A. Leninger, and J. Van de Velde, Chem. Eng. Sci. **15**, 260 (1961).

[5] R. M. Nedderman, U. Tüzün, S. B. Savage, and G. T. Houlsby, Chem. Eng. Sci. **37**, 1597 (1982).

[6] I. I. Kotchanova, Powder Technol. **4**, 32 (1970).

[7] P. W. Cleary and M. L. Sawley, Appl. Math. Mod. **26**, 89 (2002).

[8] B. J. Crewdson, A. L. Ormond, and R. M. Nedderman, Powder Technol. **16**, 197 (1977).

[9] R. L. Brown, Nature (London) **191**, 458 (1961).

[10] R. A. Altenkirch and R. Eichhorn, AIChE J. **27**, 593 (1981).

[11] J. Holland, J. E. P. Miles, C. Schofield, and C. A. Shook, Trans. Inst. Chem. Eng. Chem. Eng. **47**, 154 (1969).

[12] A. J. Carleton, Powder Technol. **6**, 91 (1972).

[13] D. Barletta, G. Donsi, G. Ferrari, and M. Poletto, Chem. Eng. Sci. **58**, 5269 (2003).

[14] G. J. Weir, Chem. Eng. Sci. **59**, 149 (2004).

[15] A. Anand, J. S. Curtis, C. R. Wassgran, B. C. Hancock, and W. R. Ketterhagen, Chem. Eng. Sci. **63**, 5821 (2008).

[16] W. Resnick, Trans. Inst. Chem. Eng. Chem. Eng. **50**, 289 (1972).

[17] P. U. Bulsara, F. A. Zenz, and R. S. Eckert, Ind. Eng. Chem. Process. Des. Dev. **3**, 348 (1964).

[18] I. R. McDougall and A. C. Evans, Rheol. Acta **4**, 218 (1965).

[19] L. S. Leung, P. J. Jones, and T. M. Knowlton, Powder Technol. **19**, 7 (1978).

[20] J. P. Boyd, Appl. Math. Lett. **11**, 27 (1998).

[21] D. A. Barry, J. Y. Parlange, L. Li, H. Prommer, C. J. Cunningham, and F. Stagnitti, Math. Comp. Simul. **53**, 95 (2000).

[22] P. A. Cundall and O. D. L. Strack, Geotechnique **29**, 47 (1979).

[23] A. V. Potapov and C. S. Campbell, Phys. Fluids **8**, 2884 (1996).

[24] J. M. F. G. Holst, J. M. Rotter, J. Y. Ooi, and G. H. Rong, J. Engng. Mech.-ASCE **125**, 104 (1999).

[25] H. P. Zhu and A. B. Yu, J. Phys. D **37**, 1497 (2004).

[26] J. Lai, P. A. Langston, C. Webb, and T. Dyakowski, Chem. Eng. Sci. **59**, 5917 (2004).

[27] H. Abou-Chakra, J. Baxter, and U. Tüzün, Adv. Powder Technol. **15**, 63 (2004).

[28] J. E. Hilton and P. W. Cleary, Phys. Fluids **2**, 071701 (2010).

[29] Y. Tsuji, T. Kawaguchi, and T. Tanaka, Powder Technol. **77**, 79 (1993).

[30] P. A. Langston, U. Tüzün, and D. M. Heyes, Chem. Eng. Sci. **49**, 1259 (1994).

[31] R. M. Nedderman, *Statics and Kinematics of Granular Materials* (Cambridge University Press, New York, 1992).

[32] Y. Guo, K. D. Kafui, C. Y. Wu, C. Thornton, and J. P. K. Seville, AIChE **55**, 49 (2009).

[33] R. Di Felice, Int. J. Multiphase Flow **20**, 153 (1994).

[34] A. Holzer and M. Sommerfeld, Powder Technol. **184**, 361 (2008).

[35] T. B. Anderson and R. Jackson, Ind. Eng. Chem. Fundam. **6**, 527 (1967).

[36] D. K. Kafui, C. Thornton, and M. J. Adams, Chem. Eng. Sci. **57**, 2395 (2002).

[37] J. E. Hilton, L. R. Mason, and P. W. Cleary, Chem. Eng. Sci. **65**, 1584 (2010).

[38] J. E. Hilton and P. W. Cleary, Chem. Eng. Sci. **66**, 231 (2011).

[39] M. Möbius, Phys. Rev. E **74**, 051304 (2006).

[40] S. Courrech du Pont, P. Gondret, B. Perrin, and M. Rabaud, Phys. Rev. Lett. **90**, 044301 (2003).